Research Square

Preprints are preliminary reports that have not undergone peer review.
They should not be considered conclusive, used to inform clinical practice,
or referenced by the media as validated information.

Hydrological Sensitivity and the Reorganization of Precipitation with Temperature over the Tibetan Plateau

Jesufemi Olowe

jesufemi@itpcas.ac.cn

Institute of Tibetan Plateau Research

LAN CUO

Institute of Tibetan Plateau Research

Article

Keywords: Tibetan Plateau, hydrological sensitivity, CMIP6, precipitation extremes, temperature–precipitation coupling, hydroclimate

Posted Date: June 19th, 2026

DOI: https://doi.org/10.21203/rs.3.rs-9863061/v1

License: This work is licensed under a Creative Commons Attribution 4.0 International License. Read Full License

Additional Declarations: No competing interests reported.

Abstract

Understanding how precipitation responds to temperature change is critical for interpreting hydroclimate risk over the Tibetan Plateau, a high-elevation water tower supplying major Asian river systems. While global-mean precipitation increases more slowly than Clausius–Clapeyron moisture scaling, regional responses can vary strongly with circulation and topography. We assess precipitation–temperature coupling over the Tibetan Plateau using two complementary approaches. First, we quantify Tibetan Plateau hydrological sensitivity (TPHS) from 14 CMIP6 models using idealized 1pctCO_2 and PiControl experiments (1850–1999), defined as the percentage change in precipitation per degree of warming. Second, we diagnose temperature-conditioned reorganization of daily precipitation occurrence using a quality-controlled 0.25° gridded observational dataset (1970–2019), evaluating precipitation intensity percentiles conditioned on temperature percentiles. The ensemble-mean TPHS is positive and seasonally varying: 3.6 ± 0.2% $°C^{-1}$ annually, with seasonal values of 2.6 ± 0.7 (winter), 4.9 ± 0.4 (spring), 3.6 ± 0.3 (summer), and 3.1 ± 0.5% $°C^{-1}$ (autumn). Observations show a systematic redistribution toward heavier daily intensities under warmer temperature regimes, most pronounced in spring and autumn. Together, these findings indicate that warming is associated with both an enhanced regional-mean precipitation response in CMIP6 models and a shift toward more frequent high-intensity precipitation in observations over the Tibetan Plateau.

1. Introduction

Precipitation is an essential element of the climate system and the global water cycle [1]. It is the principal source of freshwater and plays a central role in water-resource management and agriculture [2]. Variations in precipitation, especially extremes, can generate floods during periods of excessive rainfall or droughts during prolonged scarcity, with major environmental and socioeconomic consequences [1, 2]. Precipitation also shapes land–atmosphere and hydrologic processes by sustaining soil moisture, replenishing groundwater, and driving runoff and streamflow, which can indirectly influence erosion and pollutant transport [1, 2]. Given this importance, understanding how precipitation responds to temperature change is fundamental for interpreting hydroclimate risks under ongoing global warming.

Thermodynamically, the Clausius–Clapeyron (C–C) relationship describes the temperature dependence of saturation vapor pressure, implying that the atmospheric moisture-holding capacity increases by approximately 7% per °C under conditions of constant relative humidity and no moisture limitation [3, 4, 5]. Because precipitation intensity is closely tied to available atmospheric moisture, enhanced moisture transport can contribute to more intense precipitation events [6].

In contrast to this event-scale thermodynamic scaling, changes in global-mean precipitation and evaporation known as hydrological sensitivity are more strongly constrained by the atmospheric and surface energy budgets, yielding a slower rate of increase on the order of ~ 2–3% per °C [7, 8, 9, 10]. This energetic constraint arises because a warming atmosphere radiates energy more efficiently, particularly toward the surface, and the associated increase in atmospheric radiative cooling must be balanced primarily by increased latent heating linked to precipitation and evaporation, and to a lesser extent, sensible heat flux [11, 12, 13]. Together, these relationships connect precipitation change to temperature. Meanwhile, while these global estimates are well established, regional hydrological sensitivity can differ substantially because of circulation regimes, land–atmosphere coupling, and topographic effects, motivating region-specific analyses.

The Tibetan Plateau (TP, Fig. 1a) is a particularly important region for investigating precipitation response to warming. The Plateau spans approximately 2.5 million km^2 and has an average elevation of about 4000 m, often referred to as “the Third Pole” or the “Roof of the World” [14, 15]. Its terrain and large-scale thermal and dynamic forcing exert strong influence on regional climate and atmospheric circulation over China, Asia, and the Northern Hemisphere [14, 16]. The

Plateau is the headwater of several major Asian rivers including the Indus, Ganges, Brahmaputra, Yangtze, Yellow, and Lancang–Mekong [17, 18, 19], and extensive cryospheric components (glaciers, snow cover, permafrost) that support downstream livelihoods of more than 1.4 billion people [17, 20]. Owing to its critical role in the hydrological cycle, it is widely described as the “Asian Water Tower” [21]. Recent studies indicate that the Tibetan Plateau has experienced a significant warming trend, reaching nearly twice the global average (approximately 0.4°C per decade) [22, 23, 24]. This amplified warming has profound implications for regional and downstream water resources [25, 26]. Therefore, understanding precipitation dynamics in the context of continued warming is essential.

Climatically, the TP is influenced by the Indian monsoon, the East Asian monsoon, and the mid-latitude westerlies [16, 27]. The monsoon systems dominate the summer climate, while the westerlies exert stronger control in winter [19]. The Plateau exhibits strong spatial gradients: the southeast is generally warm and humid, whereas the northwest is cold and arid [28], with annual average precipitation decreasing from over 2000 mm in the southeast to about 20 mm in the northwest (Qaidam Basin) [29]. Distinct wet and dry seasons occur across the region [30], with summers typically wet and warm and winters cold and dry [14, 18].

Recent observational studies have documented heterogeneous trends in precipitation and its extremes across the Plateau. For example, Ge et al. [29] and Ding et al. [25] reported spatially varying changes in extreme precipitation where the wet southeast is trending dry, while the dry center and northwest are trending wet. Over 1988–2015, Xiong et al. [18] found significant increases in indices such as consecutive dry days, the simple daily intensity index, and precipitation from extremely wet days across much of the Plateau, with decreasing trends in parts of the southeast, consistent with Ding et al. [25]. Our preliminary analysis of spatial patterns and trends support the above literature as we find that precipitation ranges between 10 and 2300 mm on the TP, with a southeast–northwest precipitation gradient (Fig. 1b) while obvious precipitation decline is observed in the southeast and increase in the west and central is observed (Fig. 1c).

Despite this progress, key gaps remain in understanding precipitation–temperature coupling over the Plateau. While hydrological sensitivity has been widely studied from a global perspective, little to no work has quantified the Plateau’s hydrological sensitivity with attention to its seasonal structure. In addition, although changes in precipitation and extremes have raised concerns for water resources [25, 29, 18], there remains limited research on how precipitation intensity and frequency responds to temperature variations over the Plateau. Furthermore, many previous studies have relied on station networks that are spatially uneven, with sparse coverage in the western and northwestern Plateau, limiting robust Plateau-wide inference. This motivates the use of spatially complete observation-based gridded dataset and complementary model-based diagnostics to better understand precipitation response to warming across the plateau over the past decades.

Accordingly, this study investigates precipitation–temperature coupling over the Tibetan Plateau using two approaches. First, we quantify Tibetan Plateau Hydrological Sensitivity (TPHS) from 14 CMIP6 models using idealized 1pctCO_2 and PiControl experiments (1850–1999). Second, we examine temperature-dependent changes in precipitation frequency and intensity using station-based gridded daily temperature and precipitation data for 1970–2019. Guided by this dual framework, we ask: (i) how does TPHS vary annually and seasonally across the Plateau, (ii) how does TPHS compare with global hydrological sensitivity estimates, and (iii) how does precipitation frequency and intensity respond to temperature across seasons? By integrating idealized model experiments with observation-based analysis, this study provides a regionally focused assessment of hydroclimate sensitivity in a complex high-elevation environment.

2. Results

2.1 Tibetan Plateau Hydrological Sensitivity from CMIP6

Figure 2 summarizes TPHS values averaged over the entire Plateau for each model and the multi-model ensemble mean, shown for annual and seasonal estimates. The ensemble-mean TPHS is positive annually (3.6 ± 0.2% $°C^{-1}$) and remains positive across seasons: winter 2.6 ± 0.7% $°C^{-1}$, spring 4.9 ± 0.4% $°C^{-1}$, summer 3.6 ± 0.3% $°C^{-1}$, and autumn 3.1 ± 0.5% $°C^{-1}$. These values indicate that, in most CMIP6 models, TP-mean precipitation increases with warming, broadly consistent with energetic constraints linking warming, enhanced atmospheric radiative cooling, and latent heat release through precipitation [11].

Inter-model spread is substantial and varies by season. The spread is largest in spring (standard deviation 2.1), followed by winter (1.6) and summer/autumn (1.5), with the smallest spread in the annual mean (1.3). Spring exhibits both the largest ensemble mean sensitivity and the largest inter-model spread, indicating that transitional-season precipitation response is comparatively uncertain across models. While most models show positive TPHS across seasons, MPI-ESM1-2-HR exhibits a slightly negative winter TPHS (− 1.1 ± 0.6% $°C^{-1}$) despite positive sensitivities in other seasons, emphasizing that wintertime precipitation response remains less robust across models.

2.2 Temperature-conditioned reorganization of daily precipitation frequency (1970–2019)

To diagnose how precipitation characteristics reorganize across temperature regimes, we evaluate the relative frequency of precipitation intensity percentiles (10th_P to 100th_P) conditioned on temperature percentiles (20th_T to 100th_T) using the percentile-binning framework described in the Methods section. Results are presented for annual and seasonal analyses (Fig. 3), with supporting values in Table 2.

Table 2

Relative frequency (%) of daily precipitation intensity conditioned on temperature percentile bins over the Tibetan Plateau (1970–2019). Values are shown for each intensity class (10th_P to 100th_P) and temperature bin (20th_T to 100th_T), for annual, winter (DJF), spring (MAM), summer (JJA), and autumn (SON).

	Precipitation Percentile									
	10th_P	**20th_P**	**30th_P**	**40th_P**	**50th_P**	**60th_P**	**70th_P**	**80th_P**	**90th_P**	**100th_P**
Tmean Percentile	**Annual**									
20th_T	41.87	32.15	28.45	24.19	20.38	16.80	13.32	10.23	7.34	4.63
40th_T	21.61	23.21	22.98	22.61	21.94	21.09	19.66	18.11	15.81	12.77
60th_T	14.03	16.77	17.91	19.14	20.25	21.21	22.08	23.12	23.60	23.14
80th_T	11.57	14.32	15.75	17.52	19.11	20.87	22.82	24.40	26.37	28.35
100th_T	10.91	13.56	14.90	16.55	18.33	20.04	22.13	24.14	26.88	31.11
	Winter									
20th_T	21.09	21.61	20.38	21.00	20.08	20.71	21.09	21.38	20.41	16.53
40th_T	20.56	20.74	20.81	19.98	20.22	19.43	19.84	20.06	19.80	19.42
60th_T	20.25	20.19	20.24	20.03	20.16	19.07	19.33	19.30	19.93	20.69
80th_T	19.58	19.82	19.56	19.57	20.02	20.32	20.39	19.29	19.79	19.85
100th_T	18.52	17.64	19.00	19.43	19.51	20.48	19.36	19.96	20.06	23.51
	Spring									
20th_T	30.87	25.99	22.65	21.98	20.89	19.89	18.66	17.14	14.60	10.88
40th_T	22.42	21.98	21.15	20.74	19.99	20.05	18.95	19.42	18.48	16.70
60th_T	18.55	18.94	19.82	19.94	20.28	20.29	20.80	20.66	20.33	19.73
80th_T	15.28	16.94	18.69	19.06	19.75	20.03	20.97	21.33	22.52	24.56
100th_T	12.88	16.15	17.69	18.29	19.09	19.74	20.63	21.44	24.07	28.14
	Summer									
20th_T	22.08	21.40	21.18	20.86	20.56	20.19	20.08	19.61	18.58	18.76
40th_T	19.66	20.06	20.15	20.43	20.72	20.43	20.77	20.17	19.86	19.31
60th_T	19.64	19.78	19.96	19.88	19.89	20.13	19.99	20.24	20.54	20.09
80th_T	19.35	19.22	19.21	19.43	19.55	19.69	19.92	20.43	20.77	21.21
100th_T	19.27	19.54	19.50	19.40	19.28	19.57	19.24	19.54	20.25	20.64
	Autumn									
20th_T	33.52	29.02	26.49	22.75	20.61	17.70	16.16	13.02	11.31	9.59
40th_T	20.97	21.21	21.38	21.43	20.92	20.71	19.57	19.49	17.27	16.18
60th_T	17.35	18.19	18.36	19.89	20.43	21.41	21.31	21.24	20.91	20.82

	Precipitation Percentile									
	10th_P	20th_P	30th_P	40th_P	50th_P	60th_P	70th_P	80th_P	90th_P	100th_P
Tmean Percentile	**Annual**									
80th_T	14.44	16.23	17.61	18.22	19.48	20.47	21.37	23.36	25.02	24.55
100th_T	13.73	15.37	16.16	17.71	18.56	19.70	21.59	22.90	25.49	28.86

2.2.1 Annual

On the annual timescale (Fig. 3a), precipitation frequency shifts systematically toward higher intensities as temperature percentiles increase. Low-intensity precipitation (10th–30th_P) occurs more frequently in cooler temperature bins (20th_T and 40th_T), whereas high-intensity precipitation (90th–100th_P) becomes more frequent in warmer bins (80th_T and 100th_T). For example, the frequency of 10th_P decreases from 41.87% at 20th_T to 10.91% at 100th_T, while 100th_P increases from 4.63% at 20th_T to 31.11% at 100th_T (Table 2). This opposite temperature dependence of low versus high precipitation intensities indicates a redistribution of daily precipitation occurrence toward heavier events under warmer temperature regimes.

Spatially (Fig. 4a), low-intensity precipitation (e.g., 10th_P) shows broader and denser frequency coverage under cooler temperature bins (e.g., upper left panel), while high-intensity precipitation (e.g., 100th_P) expands and becomes more frequent over larger areas as temperature percentiles rise (e.g., lower right panel). Together, these results indicate that warmer temperature regimes are associated with a more frequent occurrence of high-intensity daily precipitation.

2.2.2 Seasonal

Winter (Fig. 3b) shows relatively modest reorganization across temperature bins. The frequency of 10th_P decreases slightly from 21.09% (20th_T) to 18.52% (100th_T), while 100th_P increases from 16.53% to 23.51% (Table 2). The comparatively muted response suggests weaker temperature-regime contrasts and/or moisture limitations during winter. Spatially, the winter maps (Fig. 4b) show small changes in frequency density across temperature bins for most precipitation percentiles, indicating that winter temperature changes only weakly reshape the spatial distribution of precipitation frequency across the Plateau.

Spring (Fig. 3c) exhibits a pronounced redistribution of precipitation frequency with temperature. 10th_P declines from 30.87% at 20th_T to 12.88% at 100th_T, while 100th_P increases from 10.88% to 28.14% (Table 2). These results indicate strong temperature dependence in the occurrence of different precipitation intensities during the spring transitional season. Spatially, Fig. 4c corroborates this pattern: the spatial density of low-intensity precipitation (e.g., 10th_P) declines as temperature percentiles increase, while high-intensity precipitation (e.g., 100th_P) becomes more spatially extensive and frequent under warmer temperature bins across much of the Plateau.

Summer (Fig. 3d) shows a comparatively weak temperature-conditioned reorganization similar to winter. 10th_P decreases only slightly from 22.08% (20th_T) to 19.27% (100th_T), while 100th_P increases marginally from 18.76% to 20.64% (Table 2). The muted response suggests limited temperature-regime contrasts during precipitation events in summer. Spatially, the summer maps (Fig. 4d) similarly show slight-to-negligible changes in precipitation-frequency patterns across temperature bins for most intensity classes, consistent with the weak dependence evident in Fig. 3d.

Autumn (Fig. 3e) shows strong temperature dependence comparable to spring. 10th_P declines from 33.52% at 20th_T to 13.73% at 100th_T, while 100th_P increases from 9.59% to 28.86% (Table 2). These results indicate pronounced

redistribution toward heavier precipitation occurrence under warmer temperature regimes during autumn. Spatially, Fig. 4e shows a widespread decline in the frequency density of low-intensity precipitation under warmer temperature bins and a corresponding expansion of high-intensity precipitation frequency, indicating Plateau-wide reorganization during this transitional season. Overall, the strongest temperature-conditioned redistribution occurs in spring and autumn, while winter and summer exhibit comparatively modest changes

3. Discussion

The TP-mean TPHS estimate of 3.6 ± 0.2% $°C^{-1}$ is slightly higher than the commonly cited global hydrological sensitivity of ~ 2–3% per °C [7, 8, 9, 39], implying a comparatively strong precipitation response to warming over the Tibetan Plateau in CMIP6 idealized experiments. Given that the annual warming rate over the Plateau is approximately twice the global average [22, 23, 24], and that annual TPHS also exceeds the global level, the Tibetan Plateau exhibits an amplified and accelerated hydroclimate response and can be regarded as a climate change hotspot. Although previous studies have highlighted amplified temperature changes on the Tibetan Plateau [40, 23], they have primarily focused on temperature rather than precipitation. Here, by explicitly quantifying hydrological sensitivity, we provide a more comprehensive assessment of the Plateau's response to global climate change.

A plausible contributing factor to the enhanced hydrological sensitivity is amplified warming over the Plateau, which increases atmospheric moisture capacity and enhances the requirement for latent heat release under the energetic constraint framework [22, 23, 24]. Additionally, the TP's complex terrain and land–atmosphere coupling may modulate HS through convection, moisture recycling, and orographic condensation processes [41, 42, 43, 44]. Changes in large-scale circulation, such as monsoon and westerly variability, can also alter moisture transport and convergence over the Plateau [45, 46]. TPHS peaks in spring (4.9 ± 0.4% $°C^{-1}$) and is smallest in winter (2.6 ± 0.7% $°C^{-1}$), reflecting greater moisture availability and circulation shifts during the transitional season. However, attributing this enhanced spring sensitivity to specific moisture-transport or circulation processes requires additional diagnostics beyond the scope of the current analysis.

The notable inter-model spread in TPHS estimates (annual σ = 1.3; spring σ = 2.1) reflects genuine structural differences among the 14 CMIP6 models. As shown in the Taylor diagram evaluation (Supplementary Fig. S2), models exhibit substantial variability in simulating TP precipitation, with correlation coefficients ranging from 0.38 to 0.66 and normalised standard deviations spanning 2.06 to 3.09, considerably larger than those for temperature. Models that overestimate precipitation variability will therefore produce different HS slopes [47]. Additional spread arises from differences in convective parameterisation schemes, particularly consequential on the TP where deep convection is frequent [48], and from the wide range of model horizontal resolutions (50–500 km), which affects orographic precipitation representation [49]. Despite this spread, the consistently positive ensemble response across all but one model-season combination supports the robustness of the 3.6% $°C^{-1}$ estimate.

Multiple studies report that precipitation intensity and the frequency of intense events tend to increase with warming due to thermodynamic moistening and circulation changes [50, 51, 52]. Consistent with this literature, our results show an opposite temperature dependence between low and high precipitation intensities, broadly consistent with Clausius–Clapeyron expectations [53]. A key finding is that the strongest temperature-conditioned redistribution occurs in spring and autumn, while winter and summer show comparatively muted changes. A plausible explanation is that spring and autumn have substantially higher temperature variability than winter and summer, increasing contrasts among temperature percentile bins. To characterize this variability, we computed the seasonal coefficient of variation (CV) of daily temperature after converting to Kelvin and removing the linear trend (see Methods). The resulting CV values confirm that autumn (CV 1.67%) and spring (CV 1.49%) exhibit greater relative variability than winter (CV 0.96%) and summer (CV 0.56%), with the annual CV at 2.43% (Table 3). Following the interpretation proposed by Nordling et al. [51],

these differences in temperature variability provide a physically consistent explanation for why precipitation-frequency changes across temperature regimes are stronger in spring and autumn.

Table 3
Seasonal coefficient of variation (CV, %) of daily mean temperature over the Tibetan Plateau (1970–2019). Temperature was converted to Kelvin (K = °C + 273.15) and linearly detrended using OLS regression before computing CV as the ratio of the standard deviation of the detrended residuals to the Kelvin mean.

Season	Temperature CV (%)
Annual	2.43
Winter	0.96
Spring	1.49
Summer	0.56
Autumn	1.67

In addition to thermodynamics, seasonal circulation regimes likely contribute. Winter precipitation is often associated with westerly disturbances under relatively low moisture content, limiting temperature-conditioned redistribution. Spring and autumn are transitional seasons (monsoon onset and retreat) during which circulation shifts may interact with temperature-regime contrasts to amplify changes in precipitation occurrence. Summer precipitation is strongly influenced by monsoon moisture transport and local evapotranspiration; however, comparatively stable warm-season temperatures may reduce contrasts among temperature percentiles, yielding a weaker signal.

It is important to note that TPHS and precipitation-frequency reorganization are derived from different data sources and characterize different facets of precipitation response to temperature. TPHS from CMIP6 idealized experiments provides a constraint-based measure of long-term precipitation response to forced warming, whereas the observational analysis diagnoses how daily precipitation occurrence shifts across temperature regimes in the realized climate. These perspectives are therefore complementary rather than directly comparable. Together, they show that (i) the regional-mean precipitation response to warming over the Plateau is positive and seasonally varying, and (ii) warmer temperature regimes are associated with a redistribution toward more frequent high-intensity daily precipitation, particularly in spring and autumn.

In summary, this study provides a dual-framework assessment of precipitation–temperature coupling over the Tibetan Plateau. Regional TPHS is positive and seasonally varying, with the 14-model ensemble mean of 3.6 ± 0.2% $°C^{-1}$ annually exceeding global estimates. Spring exhibits the highest sensitivity (4.9 ± 0.4% $°C^{-1}$) and greatest inter-model spread. Daily precipitation occurrence reorganizes systematically toward heavier intensities under warmer temperature regimes, with the strongest redistribution in spring and autumn consistent with higher seasonal temperature variability. These results collectively indicate that warming over the Tibetan Plateau is associated with both an enhanced regional-mean precipitation response and a shift toward more frequent high-intensity precipitation during key transitional seasons, with important implications for water resource management and flood risk assessment across the Asian Water Tower.

4. Methods

4.1 Idealized experiments for hydrological sensitivity (1850–1999)

To quantify hydrological sensitivity over the TP, we used annual precipitation and mean surface temperature from 14 CMIP6 models that provided idealized simulations based on (i) the 1pctCO_2 experiment, in which CO_2 increases by 1% per year from preindustrial levels, and (ii) the preindustrial control (PiControl) experiment, which provides a baseline with fixed preindustrial greenhouse gas concentrations, allowing separation of forced response from internal variability. Model fields were regridded using bilinear interpolation to a common 0.25° × 0.25° grid and clipped to the TP domain. The first realization was used for each model (r1i1p1f1, per model availability; Table 1). To assess model performance, we evaluated each CMIP6 model against observations using historical monthly temperature and precipitation over 1970–2014 using Taylor diagrams [31] summarizing correlation coefficient (R), standard deviation (σ), and root mean square error (RMSE) [32]. Taylor diagrams and associated statistics are provided in the Supplementary Information (Figs. S1–S2; Tables S1–S2).

Table 1
List of CMIP6 Earth system models analysed in this study. including modeling center, country of origin, model name, nominal horizontal resolution, and ensemble member identifier (variant label).

S/N	Modelling Centre	Country	Model	Nominal Resolution	Variant
1	BCC - Beijing Climate Center	China	BCC-CSM2	100Km	r1i1p1f1
2			BCC-ESM1	250Km	r1i1p1f1
3	CNRM-CERFACS - Centre National de Recherches Météorologiques	France	CNRM-CM6-1-HR	50 km	r1i1p1f2
4			CNRM-CM6-1	250Km	r1i1p1f2
5			CNRM-ESM2-1	250Km	r1i1p1f2
6	EC-Earth-Consortium	Europe	EC-Earth3-CC	100Km	r1i1p1f1
7			EC-Earth3-Veg	100Km	r1i1p1f1
8			EC-Earth3-AerChem	100Km	r1i1p1f1
9	NASA-GISS - NASA Goddard Institute for Space Studies	United States	GISS E-2-1-G	250Km	r101i1p1f1
10	IPSL - Institut Pierre-Simon Laplace	France	IPSL-CM5A2-INCA	500Km	r1i1p1f1
11			IPSL-CM6A-LR	250Km	r1i1p1f1
12	MIROC - Miho Institute for Computational Science, International Research Institute of Atmospheric and Oceanic Research	Japan	MIROC-ES2L	250Km	r1i1p1f1
13	MPI-M - Max Planck Institute for Meteorology	Germany	MPI-ESM1-2-HR	100km	r1i1p1f1
14	MRI - Meteorological Research Institute	Japan	MRI-ESM2-0	100Km	r1i1p1f1

4.2 Estimation of Tibetan Plateau hydrological sensitivity (TPHS)

TPHS was estimated using annual precipitation and annual mean surface temperature from 1pctCO$_2$ and PiControl. To obtain a stable long-term signal, we applied a 10-year moving average to both temperature and precipitation [12].

TPHS was then computed as the linear slope (Eq. (1)) of the percentage change in precipitation (ΔPpct) between the two experiments relative to the corresponding change in temperature (ΔT), over 1850–1999. This 150-year period supports robust estimation by sampling both the forced trend and internal variability.

$$HS = \frac{\Delta P_{pct}}{\Delta T} \#(1)$$

$$\Delta P_{pct} = \frac{P_{1pctCO2} - P_{PiControl}}{P_{PiControl}} \times 100 \#\#(2)$$

$$\Delta T = T_{1pctCO2} - T_{PiControl} \#\#\#(3)$$

Uncertainty in TPHS was quantified using the standard error of the regression slope and is expressed as the 95% confidence interval (Equations (4)–(6)). An ensemble-mean TPHS was then calculated as the mean across models. Uncertainty for the ensemble mean was derived by converting each model's margin of error to a variance term and propagating these to obtain the ensemble variance, ensemble standard error, and a 95% confidence interval for the ensemble mean (Equations (7)–(10)).

$$Standard\ Error\ of\ Regression\ (SE_{reg}) = \sqrt{\frac{\sum (y_i - \hat{y}_i)^2}{n-2}} \#(4)$$

$$Standard\ Error\ of\ the\ Slope = \frac{SE_{reg}}{\sqrt{\sum (x_i - \bar{x})^2}} \#(5)$$

$$Margin\ of\ Error = Standard\ Error\ of\ the\ Slope \times 1.96 \#(6)$$

$$Variance_i = \left(\frac{Margin\ of\ Error_i}{1.96}\right)^2 \#(7)$$

$$Ensemble\ Variance = \frac{1}{N^2} \sum_{i=1}^{N} Variance_i \#(8)$$

$$Ensemble\ Standard\ Error = \sqrt{Ensemble\ Variance} \#(9)$$

$$Ensemble\ Margin\ of\ Error = 1.96 \times Ensemble\ Standard\ Error \#(10)$$

Where SE_{reg} is the residual standard error, y_i and $\hat{y}_i$ are the observed and predicted values of the dependent variable, respectively, x_i is the independent variable, $\bar{x}$ is its mean, and n is the sample size., N total number of ensemble sample size.

4.3 Observational precipitation and temperature dataset (1970–2019)

To characterize temperature-dependent precipitation frequency across the TP, we used daily precipitation and daily mean temperature (Tmean) calculated as the average of daily temperature maxima (Tmax) and minima (Tmin) spanning 1970–2019 from a gridded station-interpolated dataset. Stations used for interpolation were obtained from the China Meteorological Administration (CMA), the Qinghai Bureau of Meteorology, and NOAA collections, including 307 precipitation stations and > 400 temperature stations for Tmax and Tmin. The data were gridded to 0.25° resolution to support robust Plateau-wide analysis and to enable comparison with common gridded products [33, 34].

A careful quality-control procedure was applied to remove implausible values. Specifically, daily precipitation < 0 mm or > 150 mm and temperature extremes > 50.8°C or < − 50°C were removed and treated as missing [34, 25].

Horizontal interpolation employed the Synographic Mapping System (SYMAP) algorithm [35], which assigns station weights based on distance and angular distribution to reduce biases from clustered stations. The method incorporates lapse-rate adjustments (monthly-varying for temperature) and elevation-dependent precipitation adjustments, in which precipitation increases with elevation up to 4000 m and decreases above 4000 m [33, 34].

4.4 Temperature-dependent precipitation frequency across intensity classes

To examine how precipitation frequency changes across temperature regimes, we applied a percentile-binning approach. This method was designed to overcome limitations of equal-width or equal-sample binning approaches that can introduce subjective bin choices or non-uniform temperature coordinates [4, 36, 37, 38]. The percentile strategy ensures adequate samples per bin across a spatially heterogeneous region such as the TP.

Following common practice, we excluded precipitation–temperature “events” with precipitation < 0.1 mm and retained only days with precipitation ≥ 0.1 mm. Daily precipitation (1970–2019) was divided into 10 percentile bins (from < 10th to ≥ 90th at 10-percentile intervals), while daily temperature was divided into 5 percentile bins (< 20th to ≥ 80th at 20-percentile intervals). Each day was categorized by the intersection of its precipitation and temperature percentile bins. We then computed, for each grid cell, the frequency of precipitation events within each combined bin and expressed that frequency as a percentage of the corresponding precipitation bin. For example, consider a single grid cell and one wet-day event with precipitation P=20mm occurring at temperature T = 18°C. After computing percentiles for this grid cell, suppose P = 20 mm falls within the 20–30th precipitation percentile bin, and T = 18°C falls within the 40–60th temperature percentile bin. Using the upper bin edge to label bins, this event is assigned to the 30th_P–60th_T bin category. This assignment is repeated for every wet-day event at the grid cell. After binning, frequencies are computed within each precipitation class: for example, if the grid cell has 1,000 events in the 30th_P precipitation class (summing over all temperature bins), and 100 of those events fall in the 60th_T bin, then the 30th_P–60th_T cell frequency is 100/1000 = 10%. This is interpreted as 10% of 30th percentile of precipitation events occurred when temperature was in the 60th percentile at this grid cell. Finally, these percentages are computed for each grid cell and averaged across the Plateau to obtain Plateau-wide summaries.

To characterize seasonal temperature variability, daily mean temperature was first converted to Kelvin (K = °C + 273.15) and linearly detrended using ordinary least-squares (OLS) regression to remove the long-term warming trend. The coefficient of variation (CV) of daily temperature was then computed as the ratio of the standard deviation of the detrended residuals to the Kelvin mean, expressed as a percentage. Using Kelvin is methodologically appropriate because it provides a true zero point, avoiding the instability that occurs when computing CV with Celsius values whose mean approaches zero after detrending.

Declarations

Competing interests

The authors declare no competing interests.

Funding

This work was supported by the National Natural Science Foundation of China (Grant No. 42371130), the Key Research & Development Program of the Tibetan Autonomous Region (Grant No. XZ202401ZY0050), and the Qinghai Key Research, Development and Application Program (Grant No. 2024-SF-142).

Author Contribution

J.O. conceptualized the study, designed the methodology, performed all data analysis and visualization, and wrote the original manuscript. L.C. secured funding and supervised the research, provided the gridded dataset, and critically revised the manuscript. Both authors read and approved the final version of the manuscript.

Acknowledgements

The authors thank the Institute of Tibetan Plateau Research, Chinese Academy of Sciences (ITPCAS) for institutional support.

Data Availability

The station-interpolated gridded precipitation and temperature dataset used in this study is available from the National Tibetan Plateau Data Center [54]. CMIP6 model output used in this study is available through the Earth System Grid Federation [55]. The Python scripts used for data processing, statistical analysis, and figure generation are archived on Zenodo [56] and are openly available through GitHub at https://github.com/FemiPeter/precip-temp-reorganization-TP.

References

1. Michaelides, S. et al. Precipitation: measurement, remote sensing, climatology and modeling. *Atmos. Res.* **94**, 512–533. https://doi.org/10.1016/j.atmosres.2009.08.017 (2009).
2. Kidd, C. & Huffman, G. Global precipitation measurement. Meteorol. *Appl* **18**, 334–353. https://doi.org/10.1002/met.284 (2011).
3. Ali, H. & Mishra, V. Contrasting response of rainfall extremes to increase in surface air and dewpoint temperatures at urban locations in India. *Sci. Rep.* **7**, 1228. https://doi.org/10.1038/s41598-017-01306-1 (2017).
4. Chen, W., Cui, H. & Ge, Q. The spatial and seasonal dependency of daily precipitation extremes on temperature in China from 1957 to 2017. *Int. J. Climatol*. **42**, 1560–1575. https://doi.org/10.1002/joc.7332 (2022).
5. Zhang, C. Moisture source assessment and the varying characteristics for the Tibetan Plateau precipitation using TRMM. *Environ. Res. Lett.* **15**, 104003. https://doi.org/10.1088/1748-9326/abac78 (2020).
6. Hartmann, D. L. et al. Observations: atmosphere and surface. in Climate Change 2013: The Physical Science Basis. Contribution of Working Group I to the Fifth Assessment Report of the Intergovernmental Panel on Climate Change (ed (ed Field, C. B.) 159–254 (Cambridge University Press, (2013).
7. Allan, R. P., Liu, C., Zahn, M., Lavers, D. A. & Koukouvagias, E. Bodas-Salcedo, A. Physically consistent responses of the global atmospheric hydrological cycle in models and observations. *Surv. Geophys.* **35**, 533–552. https://doi.org/10.1007/s10712-012-9213-z (2014).
8. Douville, H. et al. Water cycle changes. in Climate Change 2021: The Physical Science Basis (eds Masson-Delmotte, V.) 1055–1210 (Cambridge University Press, 2021). https://doi.org/10.1017/9781009157896.010
9. Norris, J., Hall, A., Thackeray, C. W., Chen, D. & Madakumbura, G. D. Evaluating hydrologic sensitivity in CMIP6 models: anthropogenic forcing versus ENSO. *J. Clim.* **35**, 6955–6968. https://doi.org/10.1175/JCLI-D-21-0780.1

(2022).

10. O'Gorman, P. A., Allan, R. P., Byrne, M. P. & Previdi, M. Energetic constraints on precipitation under climate change. *Surv. Geophys.* **33**, 585–608. https://doi.org/10.1007/s10712-011-9159-6 (2012).
11. Allan, R. P. et al. Advances in understanding large-scale responses of the water cycle to climate change. *Ann. N Y Acad. Sci.* **1472**, 49–75. https://doi.org/10.1111/nyas.14337 (2020).
12. Kramer, R. J. & Soden, B. J. The sensitivity of the hydrological cycle to internal climate variability versus anthropogenic climate change. *J. Clim.* **29**, 3661–3673. https://doi.org/10.1175/JCLI-D-15-0431.1 (2016).
13. Previdi, M. Radiative feedbacks on global precipitation. *Environ. Res. Lett.* **5**, 025211. https://doi.org/10.1088/1748-9326/5/2/025211 (2010).
14. Kuang, X. & Jiao, J. J. Review on climate change on the Tibetan Plateau during the last half century. *J. Geophys. Res. Atmos.* **121**, 3979–4007. https://doi.org/10.1002/2015JD024457 (2016).
15. Wang, X., Pang, G. & Yang, M. Precipitation over the Tibetan Plateau during recent decades: a review based on observations and simulations. *Int. J. Climatol*. **38**, 1116–1131. https://doi.org/10.1002/joc.5246 (2018).
16. Yao, T. et al. Third Pole environment (TPE). *Environ. Dev.* **3**, 52–64. https://doi.org/10.1016/j.envdev.2012.04.002 (2012).
17. Cuo, L., Zhang, Y., Zhu, F. & Liang, L. Characteristics and changes of streamflow on the Tibetan Plateau: a review. *J. Hydrol. Reg. Stud.* **2**, 49–68. https://doi.org/10.1016/j.ejrh.2014.08.004 (2014).
18. Xiong, J. et al. Spatial and temporal patterns of the extreme precipitation across the Tibetan Plateau (1986–2015). *Water* **11**, 1453. https://doi.org/10.3390/w11071453 (2019).
19. Yang, K. et al. Recent climate changes over the Tibetan Plateau and their impacts on energy and water cycle: a review. *Glob Planet. Change*. **112**, 79–91. https://doi.org/10.1016/j.gloplacha.2013.12.006 (2014).
20. Immerzeel, W. W., van Beek, L. P. H. & Bierkens, M. F. P. Climate change will affect the Asian water towers. *Science* **328**, 1382–1385. https://doi.org/10.1126/science.1183188 (2010).
21. Xu, Z. X., Gong, T. L. & Li, J. Y. Decadal trend of climate in the Tibetan Plateau—regional temperature and precipitation. *Hydrol. Process.* **22**, 3056–3065. https://doi.org/10.1002/hyp.6955 (2008).
22. Meng, Y. et al. Sensitive temperature changes on the Tibetan Plateau in response to global warming. *Atmos. Res.* **294**, 106948. https://doi.org/10.1016/j.atmosres.2023.106948 (2023).
23. Yao, T. et al. The imbalance of the Asian water tower. *Nat. Rev. Earth Environ.* **3**, 618–632. https://doi.org/10.1038/s43017-022-00299-4 (2022).
24. You, Q. et al. Warming amplification over the Arctic Pole and Third Pole: trends, mechanisms and consequences. *Earth-Sci. Rev.* **217**, 103625. https://doi.org/10.1016/j.earscirev.2021.103625 (2021).
25. Ding, J. et al. Annual and seasonal precipitation and their extremes over the Tibetan Plateau and its surroundings in 1963–2015. *Atmosphere* **12**, 620. https://doi.org/10.3390/atmos12050620 (2021).
26. Wang, R. et al. Relationship between extreme precipitation and temperature in two different regions: the Tibetan Plateau and Middle-East China. *J. Meteorol. Res.* **33**, 870–884. https://doi.org/10.1007/s13351-019-9031-3 (2019).
27. Chen, X., Zhou, T., Wu, P. & Roberts, M. J. Better resolved orography improves precipitation simulation over the Tibetan Plateau in high-resolution models. *J. Geophys. Res. Atmos.* **129** https://doi.org/10.1029/2024JD041140 (2024). e2024JD041140.
28. Yin, Y. et al. Modelled effects of climate change on actual evapotranspiration in different eco-geographical regions in the Tibetan Plateau. *J. Geogr. Sci.* **23**, 195–207. https://doi.org/10.1007/s11442-013-1003-0 (2013).
29. Ge, G. et al. Analysis of precipitation extremes in the Qinghai-Tibetan Plateau, China: spatio-temporal characteristics and topography effects. *Atmosphere* **8**, 127. https://doi.org/10.3390/atmos8070127 (2017).

30. Li, X. et al. Seasonal evapotranspiration changes (1983–2006) of four large basins on the Tibetan Plateau. *J. Geophys. Res. Atmos.* **119**, 13,079–13105. https://doi.org/10.1002/2014JD022131 (2014).
31. Taylor, K. E. Summarizing multiple aspects of model performance in a single diagram. *J. Geophys. Res. Atmos.* **106**, 7183–7192. https://doi.org/10.1029/2000JD900719 (2001).
32. Gleckler, P. J., Taylor, K. E. & Doutriaux, C. Performance metrics for climate models. *J. Geophys. Res. Atmos.* **113**, D06112. https://doi.org/10.1029/2007JD008972 (2008).
33. Cuo, L. & Zhang, Y. Spatial patterns of wet season precipitation vertical gradients on the Tibetan Plateau and the surroundings. *Sci. Rep.* **7**, 5057. https://doi.org/10.1038/s41598-017-05199-2 (2017).
34. Cuo, L. et al. Climate change on the northern Tibetan Plateau during 1957–2009: spatial patterns and possible mechanisms. *J. Clim.* **26**, 85–109. https://doi.org/10.1175/JCLI-D-11-00561.1 (2013).
35. Shepard, D. S. Computer mapping: the SYMAP interpolation algorithm. in Spatial Statistics and Models (eds (eds Gaile, G. L. & Willmott, C. J.) 133–145 (Springer, (1984).
36. Karl, T. R. & Trenberth, K. E. Modern global climate change. *Science* **302**, 1719–1723. https://doi.org/10.1126/science.1090228 (2003).
37. Wasko, C. & Sharma, A. Quantile regression for investigating scaling of extreme precipitation with temperature. *Water Resour. Res.* **50**, 3608–3614. https://doi.org/10.1002/2013WR015194 (2014).
38. Yong, Z. et al. Relationship of extreme precipitation, surface air temperature, and dew point temperature across the Tibetan Plateau. *Clim. Change*. **165**, 1–22. https://doi.org/10.1007/s10584-021-03087-5 (2021).
39. Pendergrass, A. G. The global-mean precipitation response to CO_2-induced warming in CMIP6 models. *Geophys. Res. Lett.* **47** https://doi.org/10.1029/2020GL089964 (2020). e2020GL089964.
40. Liu, X., Cheng, Z., Yan, L. & Yin, Z. Y. Elevation dependency of recent and future minimum surface air temperature trends in the Tibetan Plateau and its surroundings. Glob. Planet. Change 68, 164–174 (2009). https://doi.org/10.1016/j.gloplacha.2009.03.017 [NOTE: this reference was missing from the original manuscript's reference list and has been added].
41. Chen, W., Cui, H. & Zheng, J. Prediction of Clausius–Clapeyron scaling of daily precipitation extremes over China. *J. Clim.* **37**, 165–177. https://doi.org/10.1175/JCLI-D-23-0030.1 (2024).
42. Fu, Y. et al. Land-surface processes and summer-cloud-precipitation characteristics in the Tibetan Plateau and their effects on downstream weather: a review and perspective. *Natl. Sci. Rev.* **7**, 500–515. https://doi.org/10.1093/nsr/nwz226 (2020).
43. Lin, Z. et al. Tibetan Plateau vortex-associated precipitation and its link with the Tibetan Plateau heating anomaly. *Int. J. Climatol*. **41**, 6300–6313. https://doi.org/10.1002/joc.7195 (2021).
44. Wan, B., Gao, Z., Chen, F. & Lu, C. Impact of Tibetan Plateau surface heating on persistent extreme precipitation events in southeastern China. *Mon Weather Rev.* **145**, 3485–3505. https://doi.org/10.1175/MWR-D-17-0061.1 (2017).
45. Jiang, X. et al. The westerly winds control the zonal migration of rainy season over the Tibetan Plateau. *Commun. Earth Environ.* **4**, 363. https://doi.org/10.1038/s43247-023-01035-6 (2023).
46. Lai, H. W. et al. Regionalization of seasonal precipitation over the Tibetan Plateau and associated large-scale atmospheric systems. *J. Clim.* **34**, 2635–2651. https://doi.org/10.1175/JCLI-D-20-0521.1 (2021).
47. Fläschner, D., Mauritsen, T. & Stevens, B. Understanding the intermodel spread in global-mean hydrological sensitivity. *J. Clim.* **29**, 801–817. https://doi.org/10.1175/JCLI-D-15-0351.1 (2016).
48. Zhao, M. et al. Uncertainty in model climate sensitivity traced to representations of cumulus precipitation microphysics. *J. Clim.* **29**, 543–560. https://doi.org/10.1175/JCLI-D-15-0191.1 (2016).

49. Zhu, Y. Y. & Yang, S. Evaluation of CMIP6 for historical temperature and precipitation over the Tibetan Plateau and its comparison with CMIP5. *Adv. Clim. Change Res.* **11**, 239–251. https://doi.org/10.1016/j.accre.2020.08.001 (2020).
50. Myhre, G. et al. Frequency of extreme precipitation increases extensively with event rareness under global warming. *Sci. Rep.* **9**, 16063. https://doi.org/10.1038/s41598-019-52277-4 (2019).
51. Nordling, K., Fahrenbach, N. L. S. & Samset, B. H. Climate variability can outweigh the influence of climate mean changes for extreme precipitation under global warming. *Atmos. Chem. Phys.* **25**, 1659–1684. https://doi.org/10.5194/acp-25-1659-2025 (2025).
52. Zhang, W. et al. Intensified response of extreme precipitation to rising temperature over the Tibetan Plateau from CMIP6 multi-model ensembles. *J. Hydrol.* **637**, 131397. https://doi.org/10.1016/j.jhydrol.2024.131397 (2024).
53. Chou, C., Chen, C. A., Tan, P. H. & Chen, K. T. Mechanisms for global warming impacts on precipitation frequency and intensity. *J. Clim.* **25**, 3291–3306. https://doi.org/10.1175/JCLI-D-11-00239.1 (2012).
54. □□ □□□□□□□0.25□□□□□□□□□□□□□□□□□□□(1957–2020) [Data set]. □□□□□□□□□□□□□: □□□□□□□□□□□□□ https://doi.org/10.11888/Atmos.tpdc.272349 (2022).
55. Eyring, V. et al. Overview of the Coupled Model Intercomparison Project Phase 6 (CMIP6) experimental design and organization. *Geosci. Model. Dev.* **9**, 1937–1958. https://doi.org/10.5194/gmd-9-1937-2016 (2016).
56. Olowe, J. FemiPeter/precip-temp-reorganization-TP: v1.0.0 — initial release. Zenodo https://doi.org/10.5281/ZENODO.20269001 (2026).

Figures

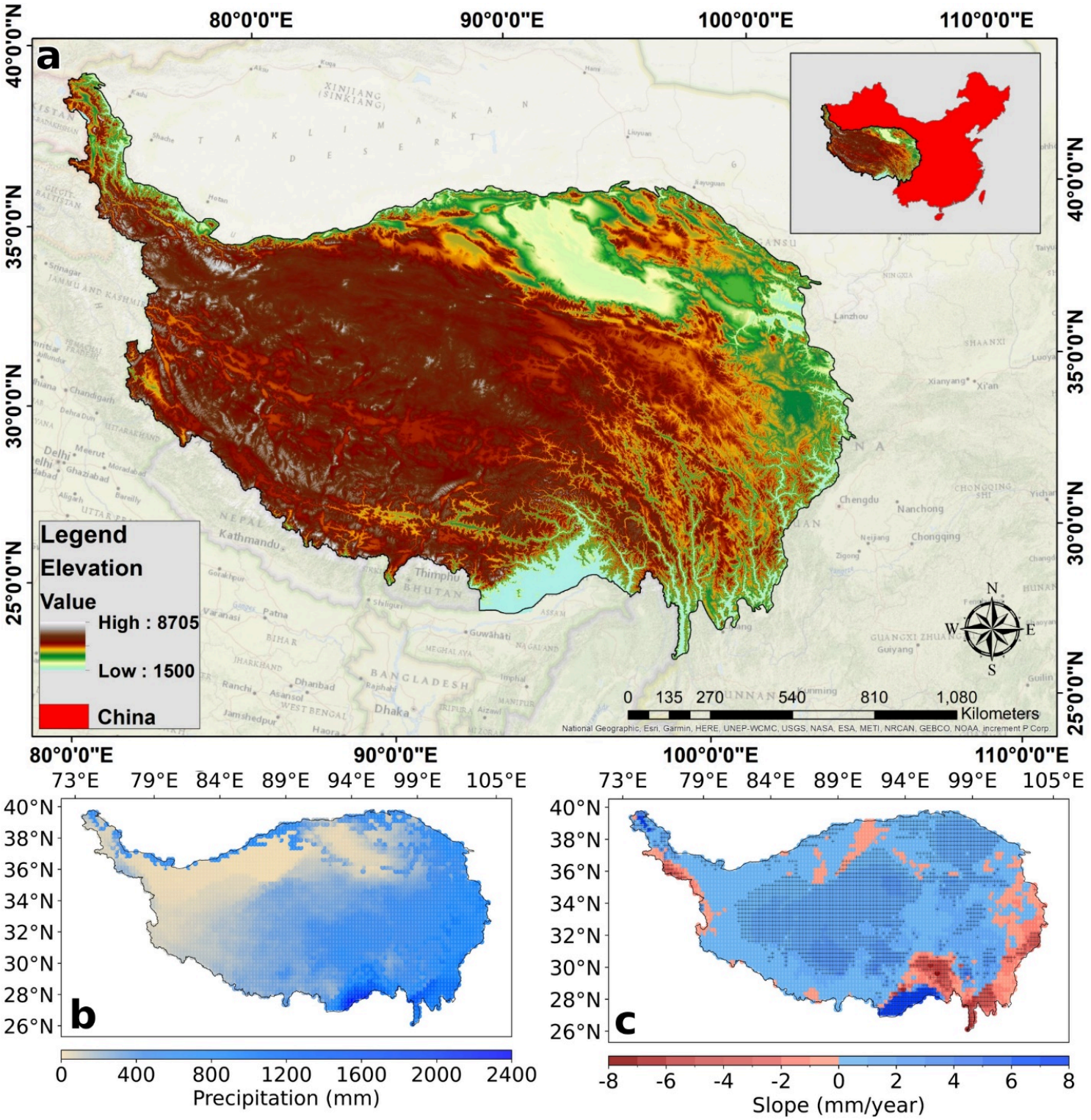


Figure 1

Study area and climatological precipitation over the Tibetan Plateau. (a) Location of the Tibetan Plateau showing topographic elevation (m a.s.l.). (b) Mean annual precipitation (mm) over the TP for 1970–2019 derived from the 0.25° station-interpolated gridded dataset, illustrating the southeast-to-northwest precipitation gradient (10–2,300 mm). (c) Spatial pattern of precipitation trends (mm year^{-1}) over 1970–2019, showing decline in the southeast and increases in the central and western Plateau.

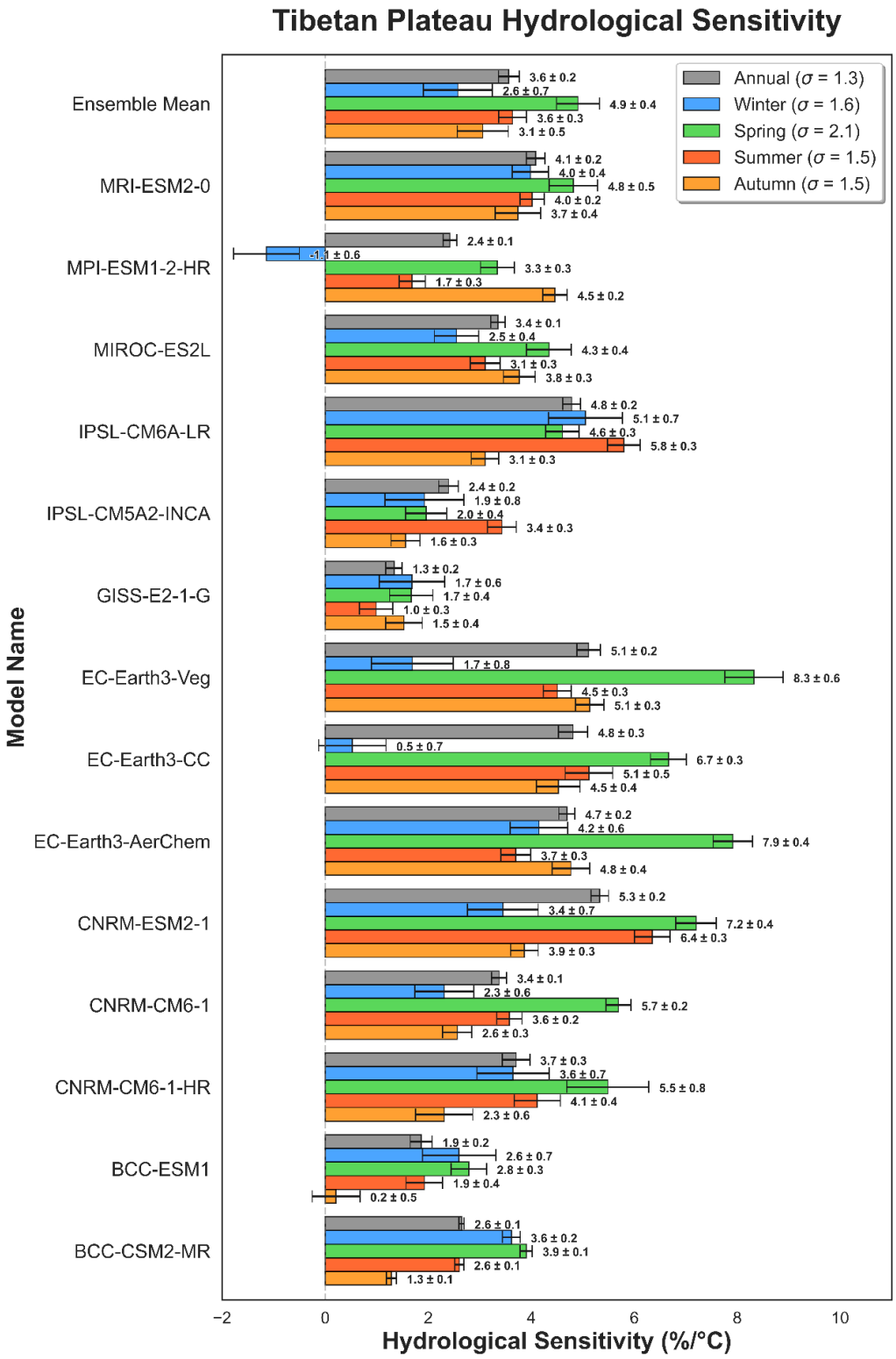


Figure 2

Annual and seasonal Tibetan Plateau Hydrological Sensitivity (TPHS; % °C⁻¹). Bars represent annual (gray), winter (blue), spring (green), summer (red), and autumn (orange) sensitivities. Error bars denote the 95% confidence interval estimated from the standard error of the regression slope. Numerical labels indicate the mean HS ± 95% margin of error for each model and season. The ensemble standard deviation (σ) across models for each season is shown in the legend.

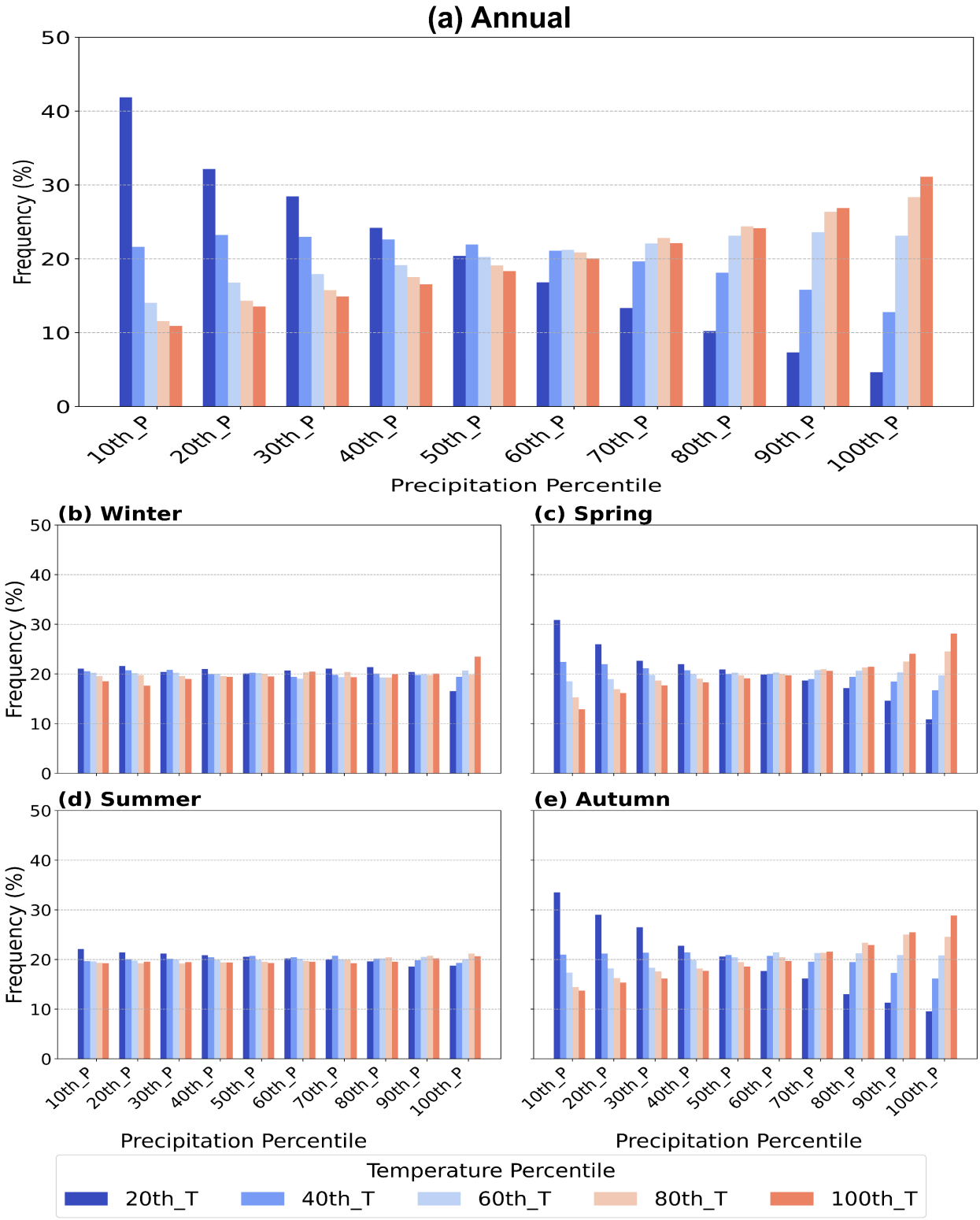


Figure 3

Reorganization of precipitation intensity (in percentiles) across temperature regimes over the Tibetan Plateau. Bars show the relative frequency (%) of precipitation percentiles (10th–100th) conditioned on temperature percentiles (20th, 40th, 60th, 80th, and 100th). Results are presented for (a) annual, (b) winter, (c) spring, (d) summer, and (e) autumn. Each panel illustrates how the distribution of precipitation intensity shifts as temperature percentiles increase, highlighting seasonal differences in precipitation–temperature coupling.

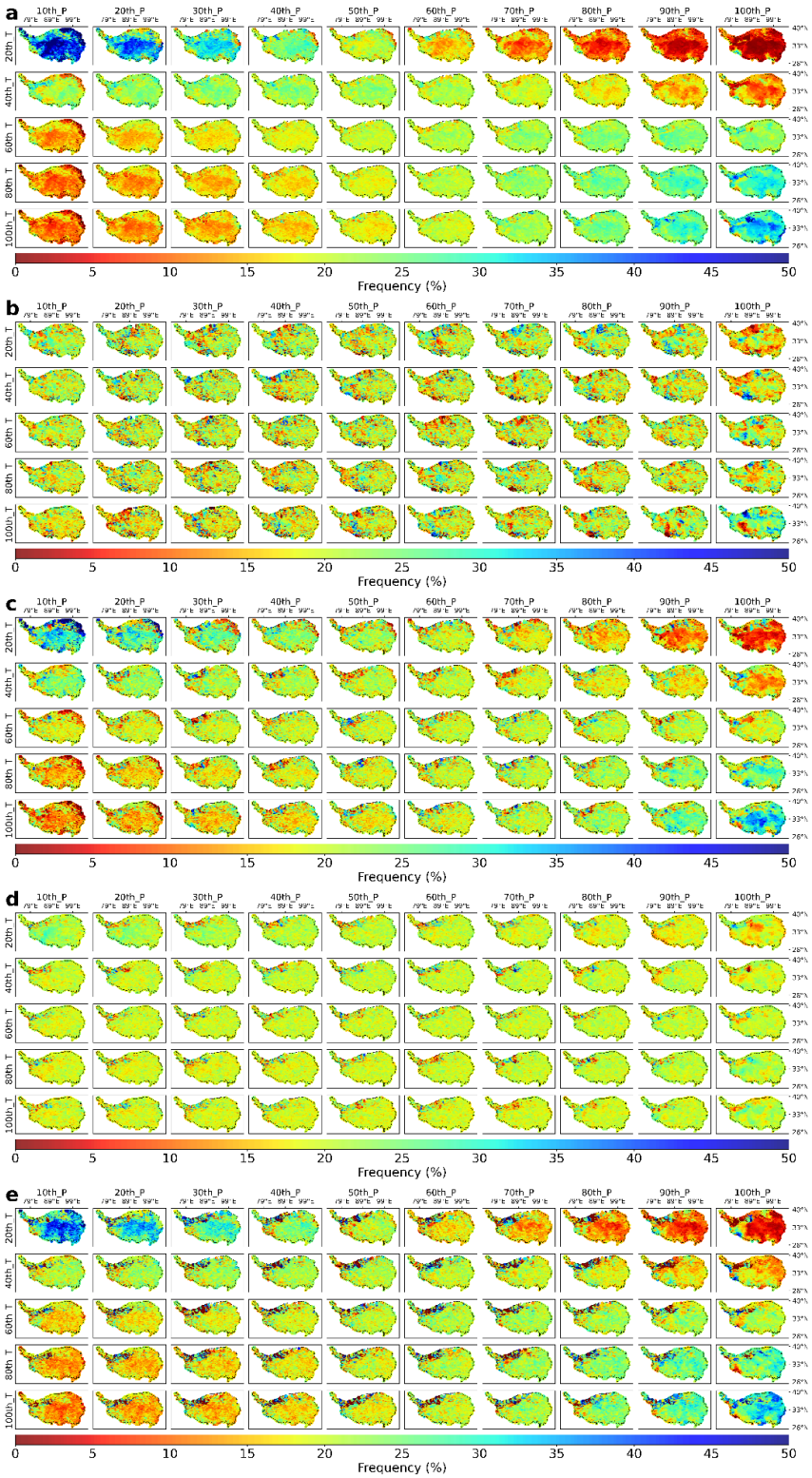


Figure 4

Spatial distribution of temperature-conditioned precipitation intensity and frequency over the Tibetan Plateau. Each panel shows the relative frequency (%) of a given precipitation intensity percentile (10th_P to 100th_P) across five temperature percentile bins (20th_T to 100th_T). Results are presented for (a) annual, (b) winter (DJF), (c) spring (MAM), (d) summer (JJA), and (e) autumn (SON). All results are derived from the 0.25° station-interpolated gridded dataset (1970–2019).

Supplementary Files

This is a list of supplementary files associated with this preprint. Click to download.

- SRSupplementaryInformation.docx